Backbone Dynamics of the Ribonuclease Binase Active Site Area Using Multinuclear (^{15}N and ^{13}CO) NMR Relaxation and Computational Molecular Dynamics†

Yuxi Pang,‡,|| Matthias Buck,§,⊥ and Erik R. P. Zuiderweg*,‡

Department of Biological Chemistry, University of Michigan, Biophysics Research Division, 930 North University Avenue, Ann Arbor, Michigan 48109-1055

Received August 14, 2001; Revised Manuscript Received December 13, 2001

ABSTRACT: The nano-pico second backbone dynamics of the ribonuclease binase, homologous to barnase, is investigated with ^{15}N, ^{13}C NMR relaxation at 11.74 and 18.78 T and with a 1.1 ns molecular dynamics simulation. The data are compared with the temperature factors reported for the X-ray structure of this enzyme. The molecular dynamics and X-ray data correspond well and predict motions in the loops 56−61 and 99−104 that contain residues that specifically recognize substrate and are catalytic (His101), respectively. In contrast, the ^{15}N relaxation data indicate that these loops are mostly ordered at the nano-pico second time scale. Nano-pico second motions in the recognition loop 56−61 are evident from ^{13}CO−^{13}Cα cross relaxation data, but the mobility of the catalytic loop 99−104 is not detected by ^{13}CO cross relaxation either. From the results of this and previous work [Wang, L., Pang, Y., Holder, T., Brender, J. R., Kurochkin, A., and Zuiderweg, E. R. P. (2001) *Proc. Natl. Acad. Sci. U.S.A.*, 98, 7684−7689], the following dynamical characterization of the active site area of binase emerges: a beta sheet, rigid at all probed time scales, supports the catalytic residue Glu 72. Both substrate-encapsulating loops are mobile on both fast and slow time scales, but the fast motions of the loop which contains the other catalytic residue, His 101, as predicted by B-factors and computational molecular dynamics is not detected by NMR relaxation. This work strongly argues for the use of several measures in the study of protein dynamics.

The characterization of protein dynamics may help to correlate structural properties with biological activities (*1*−*3*). Enzyme active sites often contain protein loops, which are by nature dynamic. Part of such a site may need to sequester a substrate, or some times even isolate it from the solvent into the protein interior (*4*−*10*). In some cases, the sequestering loops contain catalytic residues (*11*−*13*). Here we focus on the study of the dynamical behavior of the active-site area of the ribonuclease binase, using nuclear magnetic resonance (NMR)[1] spectroscopy and simulated molecular dynamics (MD). NMR spectroscopy is a powerful tool to study protein dynamics at multiple atomic-sites covering a wide range of time-scales (*14*−*17*). Molecular dynamics simulations have recently become sufficiently efficient to probe similar time scales as the NMR relaxation and can thus be used to help interpret and complement the NMR methods (*18*−*20*).

Binase is a guanyl-specific extracellular ribonuclease secreted by *Bacillus intermedius*, which catalyzes the endonucleotic cleavage of single-stranded RNA (*21*). It consists of a single polypeptide chain (109 amino acid residues) that is folded into a $\alpha+\beta$ compact structure as determined by X-ray crystallography and NMR spectroscopy (*22*−*24*). The tertiary structure of binase is virtually superimposable with that of the well-studied enzyme barnase, a homologue with 85% sequence identity (*25*, *26*). As shown in Figure 1, three α helices are located in the N terminal part of binase, while five antiparallel β strands are in the C terminal part. Of the two catalytic residues, Glu 72 is located on the "bottom" of the active site cleft on strand β2, while His 101 is perched on the loop L5 connecting strands β4 and β5. Loop L2, formed by residues 56−67 connecting the first and second β sheet, is responsible for the binding of the guanine group of the substrate. The interactions between loop L2 and the substrate, in particular with residues Phe 55, Arg 58, and Glu 59, contribute to the majority of the enzyme's specificity (*21*, *27*). The crystal structure of the homologous enzyme barnase with the inhibitor dCGAG suggests that the substrate in this class of enzymes is also interacting with Lys 26 of helix α2, with Tyr102 on the loop connecting strands β4 and β5, and with Arg 86 on loop L3 (binase count) (*28*).

† Supported by Grant MCB 9814431 of the National Science Foundation.

* To whom correspondence should be addressed. Phone: (734) 936-3850. Fax: (734) 764 3323. E-mail: zuiderwe@umich.edu.

‡ Biophysics Research Division, Department of Biological Chemistry and Department of Chemistry, The University of Michigan, 930 N University Avenue, Ann Arbor, MI 48109.

§ Department of Chemistry and Chemical Biology, Harvard University, 12 Oxford Street, Cambridge, MA 02139.

|| Present address: Laboratory of Functional and Molecular Imaging, 10 Center Drive, 10/B1D118, NINDS/NIH, Bethesda, MD 20892.

⊥ Present address: Memorial Sloan-Kettering Cancer Center, 1275 York Avenue, New York, NY 10021.

[1] Abbreviations: NMR, nuclear magnetic resonance; MD, molecular dynamics; CSA, chemical shift anisotropy; CPMG, Carr-Purcell-Meiboom-Gill; RMSD, root-mean-square displacement; RMSF, root-mean-square fluctuation; R_1, longitudinal spin relaxation rate; R_2, transverse spin relaxation rate; $R_{1\rho}$, rotating frame spin relaxation rate; η_{xy}, transverse cross correlation rate; NOE, nuclear Overhauser effect.

10.1021/bi011657f CCC: $22.00
Published on Web 01/30/2002

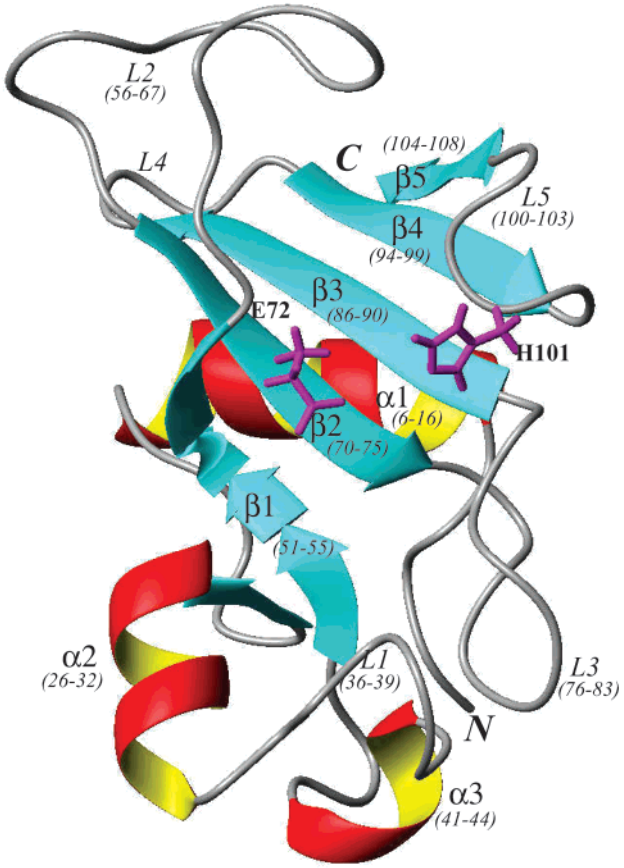

FIGURE 1: Ribbon diagram of the ribonuclease binase. The secondary structure elements (three α helixes, five antiparallel β sheets, and three loops) as well as the connecting loops are labeled, along with two catalytic residues, Glu 72 and His 101. This figure was generated from the averaged NMR structure (*24*) using the program MOLMOL (*83*).

The nano-pico second dynamical analysis of binase presented here is complementary to our recent work (*13*), which explored the milli/micro second dynamics of this protein. It was shown that binase's active site loops 55−70 and 99−104 undergo conformational exchange dynamics with a rate constant of 3000 s^{-1}, which is similar to the maximum k_{cat} of this enzyme. In contrast, the "bottom" of the active site, composed of the five-stranded beta sheet, was found to be rigid at those time scales. In the present work, we investigate whether the functionally important slow dynamical processes of the loops are accompanied by faster processes as well. We use a three-pronged approach: (i) ^{15}N NMR auto- and cross- correlation relaxation at 11.74 and 18.78 T (corresponding to 500 and 800 MHz ^{1}H), (ii) ^{13}CO−^{13}Cα cross relaxation at 18.78 T, and (iii) a 1.1 ns molecular dynamics simulation.

The results of these studies are compared with each other and with dynamical information obtained from the temperature factors reported for the crystal structure of this enzyme (*22*, *23*). While these factors contain also effects of crystal imperfection and overall librational motions, they certainly contain local dynamical information as well, on an extended range of time scales (*29*−*31*). We find that the X-ray and MD data are in reasonable agreement. Significantly, the loop containing the catalytic histidine and the base recognition loop formed by residues 55−61 are found to be very dynamic in both methods. However, the order parameters derived from the ^{15}N relaxation of binase do not agree very well with either MD simulation or X-ray B-factors. Most importantly, only little motion for the enzyme's active site region is found by this method, which would lead one to believe that no motions for this important area exist in solution. However, extensive dynamics on the nano-pico second time scale in the recognition loop 56−61 is evident from ^{13}CO−^{13}Cα cross relaxation measurements, indicating that these motions are very anisotropic. Mobility of the catalytic loop is not detected by the ^{13}CO relaxation; we conclude that this region is either confined to translational motions, and/or to motions at a much slower time scale. With the combined use of ^{15}N and ^{13}C relaxation data, we were also able to discern a fraying motion at the N-terminus of the first α helix of the protein. Interestingly, such fraying motion has been predicted in theoretical folding/unfolding experiments with the related enzyme barnase. Overall, we find that better agreement between MD, X-ray, and NMR data is obtained if ^{15}N and ^{13}C relaxation measures are combined. In addition, the comparison of all methods allows some characterization of motional models for the functionally important areas of the protein.

MATERIALS AND METHODS

NMR Experiments. ^{15}N Relaxation Rate Measurements. The spin−lattice relaxation rate R_1, spin−spin relaxation rate R_2, steady-state {^{1}H}-^{15}N heteronuclear NOE, and transverse ^{15}N chemical shift anisotropy (CSA)/^{15}N-^{1}H dipole cross correlation rates (η_{xy}) were measured on both a Bruker Avance 500 MHz and a Varian INOVA 800 MHz spectrometer. A 2.0 mM ^{15}N-labeled sample (90:10 H_2O/D_2O, pH 5.5) of binase was used in the experiments at a temperature 303 K. The pulse sequences were slightly modified from the published ones (*14*, *15*, *32*), in the sense that the water signal was kept saturated in all R_2 and R_1 experiments to avoid the progressive saturation in longer experiments with undesired saturation transfer from the bulk water. Two different pulse schemes were used to measure R_2 rates, one with the conventional Carr-Purcell-Meiboom-Gill (CPMG) sequence with multiple π pulses with a repetition rate of 4 kHz (*14*, *15*, *33*), to reduce conformational or chemical exchange effects, and the other with a spin−echo sequence using single π pulse to maximize such effects (*13*). The latter experiment, shown in Figure 2, employs composite pulse proton decoupling to suppress ^{15}N CSA/^{15}N-^{1}H dipole cross correlation, as well as the instantaneous ^{1}H-^{15}N scalar coupling evolution. It has been stated that the use of a composite pulse sequence on the protons can interfere with the ^{15}N spin−echo formation (*34*), but our results in Figure 4 indicate that this effect is minimal. The relaxation delays were 10, 50, 100, 150, 200, 300, 350, 400, and 450 ms and 5, 20, 35, 60, 85, 100, 110, 120, and 130 ms for R_1 and R_2 respectively. The length of the proton saturation for NOE measurements was 3.5 s. The NOE control experiment was collected with a 3.5 s recycle delay, and the water magnetization was restored to +z throughout. The η_{xy} experiments were carried out with cross correlation delays of 30, 40, 50, 55, and 60 ms (11.74 T) and 25, 35, 40, 45, and 50 ms (18.78 T). All experiments were duplicated at least once to estimate the experimental uncertainties.

The ^{15}N relaxation behavior could not be measured for several residues due to resonance overlap in the ^{15}N-^{1}H

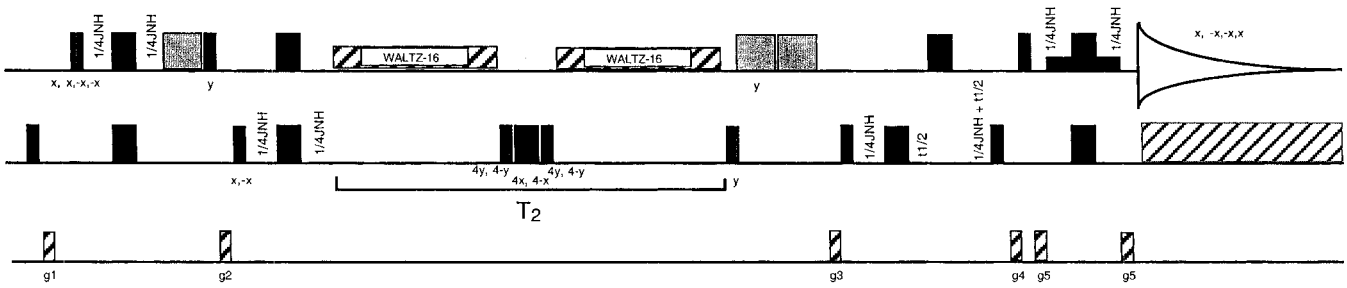

FIGURE 2: Pulse sequence for the measurement of ^{15}N R_2 relaxation with minimal suppression of the chemical/conformational exchange broadening (R_2 (spin−echo)). This is achieved by the use of only a single composite ^{15}N π pulse during the R_2 relaxation time. The composite-pulse proton decoupling suppresses ^{15}N CSA/^{15}N-^{1}H dipole cross correlation, as well as the instantaneous ^{1}H-^{15}N scalar coupling evolution. In combination with a conventional CPMG experiment, this experiment quickly identifies interesting areas of conformational/chemical exchange in biomolecules, without the need to go through a full R_1, R_2, and NOE relaxation study with the associated calculations to retrieve R_{ex} (*13*). The experiment can be modified for conventional or TROSY gradient coherence selection with sensitivity enhancement (*84*, *85*) by making the necessary substitutions after the R_2 relaxation period. An alternative sequence to obtain R_2 relaxation with minimal suppression of the chemical/conformational exchange broadening has recently been proposed by others (*86*).

fingerprint, most noticeably for the consecutive loop residues 81−83. This problem was overcome with a HNCO-style read-out for the ^{15}N R_1 and R_2 relaxation experiments, using ^{13}CO frequency labeling in a double-labeled protein (*35*). These experiments were obviously of lesser sensitivity than the standard ^{15}N relaxation experiments, but sufficed to assess the approximate dynamical properties of this loop and several other residues for which data were otherwise unavailable. No ^{1}H-^{15}N NOE experiment with HNCO read-out was carried out; hence, no order parameters were calculated for the residues with overlap problems. Residues 66 and 67 eluded detection in all experiments, most likely due to excessive conformational exchange broadening.

^{13}CO Relaxation Rate Measurements. We applied a procedure previously developed in our laboratory (*36*, *37*) which measures the cross relaxation rate between ^{13}CO and $^{13}C\alpha$ spin, $\sigma_{C\alpha-CO}$, which is independent of other dipolar relaxation mechanisms and ^{13}CO CSA tensor variations. The cross relaxation rate is obtained by measuring the steady-state {$^{13}C\alpha$}-^{13}CO homonuclear nuclear Overhauser effect (NOE) $<C_z^\alpha>_{SAT}$, a control $<C_z^\alpha>_{CTR}$, and the ^{13}CO spin−lattice relaxation rate (R_1^{CO}):

$$\sigma_{C\alpha-CO} = \frac{\langle C_z^\alpha\rangle_{SAT} - \langle C_z^\alpha\rangle_{CTR}}{\langle C_z^\alpha\rangle_{CTR}} R_1^{CO} \qquad (1)$$

The cross relaxation rate is given, using Lipari-Szabo spectral density functions (*38*) by

$$\sigma_{C\alpha-CO} = -\frac{1}{4}\left(\frac{\mu_0}{4\pi}\right)^2 \hbar^2 \gamma_C^4 \langle r_{C\alpha-CO}^{-3}\rangle^2 \times \left\{\frac{S_{C\alpha-CO}^2 \tau_C}{1+(\omega_{CO}-\omega_{C\alpha})^2\tau_C^2} + \frac{(1-S_{C\alpha-CO}^2)\tau}{1+(\omega_{CO}-\omega_{C\alpha})^2\tau^2} - \frac{6S_{C\alpha-CO}^2 \tau_C}{1+(\omega_{CO}+\omega_{C\alpha})^2\tau_C^2} - \frac{6(1-S_{C\alpha-CO}^2)\tau}{1+(\omega_{CO}+\omega_{C\alpha})^2\tau^2}\right\} \qquad (2)$$

where the symbols have their usual meaning, and where $S_{C\alpha-CO}^2$ is the order parameter describing the local reorientation of the Cα−CO internuclear vector. As usual, $1/\tau = 1/\tau_c + 1/\tau_e$, with τ_c the overall rotational correlation time and τ_e the correlation time of the local motion. At 18.78 T magnetic field (800 MHz ^{1}H) and with a rotational correlation time of 6.1 ns, as determined for binase, all but the first Lorentzians in eq 2 can be neglected, and one obtains, to very good approximation:

$$\sigma_{C\alpha-CO} \cong -\frac{1}{4}\left(\frac{\mu_0}{4\pi}\right)^2 \hbar^2 \gamma_C^4 \langle r_{C\alpha-CO}^{-3}\rangle^2 S_{C\alpha-CO}^2 \tau_C \qquad (3)$$

which becomes, for axially symmetric overall anisotropic rotation:

$$\sigma_{C\alpha-CO} \cong -\frac{1}{4}\left(\frac{\mu_0}{4\pi}\right)^2 \hbar^2 \gamma_C^4 \langle r_{C\alpha-CO}^{-3}\rangle^2 S_{C\alpha-CO}^2 \{A\tau_C^a + B\tau_C^b + C\tau_C^c\} \qquad (4)$$

where the factors A−C and the different τ_c's describe the vector orientation dependency according to Woessner theory (*39*).

The experiments were carried out with a Varian INOVA 800 MHz NMR spectrometer. A double labeled (^{13}C/^{15}N) sample of binase, at the same conditions as the single labeled sample, was used in these experiments. The HNCO-type pulse schemes were slightly modified from our previous published sequences (*36*). Currently, proton saturation was not used during the ^{13}CO relaxation delays, and a train of adiabatic pulses, instead of Gaussian pulses, was used for selective saturation of all aliphatic carbon nuclei. Two sets of R_1 experiments were recorded, each containing 10 relaxation delays (10, 100, 200, 400, 600, 600, 700, 700, 1500, and 1500 ms). Seven sets of NOE experiments were recorded, each containing two separate experiments with a 10 s adiabatic pulse train centered at 50 ppm to saturate the aliphatic carbon nuclei and one where this field was centered at 300 ppm as the control. Each 2D data set contained 2k*54 complex points, with a spectral width of 15009 and 2100 Hz in the ^{1}H and ^{13}CO dimensions. Instrumental times for R_1 rate and NOE measurements were about 50 and 70 h, respectively.

Data Analysis. All data were processed and analyzed using NMRPipe (*40*) and NMRView (*41*) programs. Before Fourier transformation of the raw data, a Lorentzian-to-Gaussian and a cosine-squared window function along direct (^{1}H) and

indirect (^{15}N or ^{13}CO) dimension were applied, and the data were then zero-filled to 4K*512 (8K*1024) for ^{15}N (^{13}CO) relaxation data. Experimental uncertainties were estimated from the seven duplicate spectra for NOE experiments, while for R_1 and R_2 experiments, the errors were obtained from a Monte Carlo simulation using synthetic data sets following a Gaussian distribution (*42*, *43*). Order parameters S^2 (^{15}N−H) were determined by fitting the ^{15}N relaxation data at 11.74 T (R_1, R_2, and NOE) and 18.78 T (NOE and R_1), using the program Modelfree (*44*) in which different dynamic models were chosen for different spins to describe the relaxation behavior.

In this study, the carbonyl atoms are assigned the residue number corresponding to the following residue.

Molecular Dynamics Simulation. Simulation Protocol. A molecular dynamics (MD) simulation of solvated binase was performed using the program CHARMM (*45*) with an all-atom Param22 potential function (*46*). The simulation protocol was almost the same as that for the simulation of lysozyme (*47*). The atom initial coordinates of the system were taken from the X-ray crystal structure (2.5 Å resolution) of binase (*23*). Hydrogen atoms were added using the subroutine HBUILD in CHARMM. To mimic the actual experimental conditions, the ionizable side groups were properly charged, depending on their corresponding pK_a values. Both electrostatic and van der Waals forces were treated with the force switch method, with a switching range of 9−11.5 Å (*48*), while the nonbonded list was kept to 13.5 Å and updated heuristically.

After initial energy minimization, the protein was solvated by placing it at the center of a 30 Å sphere of TIP3P waters (*49*, *50*). The water molecules that overlapped with the protein were eliminated and 3232 water molecules were left consisting of 85% atoms in the final system. A stochastic boundary potential was applied to the solvent molecules (*51*) and the SHAKE algorithm was applied to restrain the hydrogen atoms in the water molecules (*52*).

The water molecules were first minimized and then briefly equilibrated around the protein by a 4 ps dynamics simulation. Random velocities were assigned to all atoms in accordance with a Maxwell−Boltzmann distribution at 53 K; subsequently, the system was heated slowly to 303 K and equilibrated for additional 14 ps. The constant temperature of the system was maintained by the novel NOSE-HOOVER thermostat (*53*, *54*).

The atom positions were propagated for 1.6 ns by a multiple time step (MTS) ds-RESPA method using a velocity Verlet algorithm (*55*, *56*). Bond and angle, improper and dihedral, and all other forces were updated at time steps of 0.5, 2, and 4 fs intervals, respectively. Short- versus long-range force selection was employed with a cutoff of 6.0 Å. The energy, radius of gyration, and the drift of atoms from a reference structure (RMSD) all leveled off within the first 500 ps of the MD simulation (see Figure 3). Only the trajectory data between 600 and 1600 ps, thus representing a 1.1 ns equilibrium run, was used for the data analysis reported here. The total MD run took about 700 h of CPU time using a SGI Octane workstation (R10000), in which the atom coordinates were saved every 0.2 ps.

Data Analysis. The structure comparisons are made by calculating the root-mean-square deviation (RMSD)

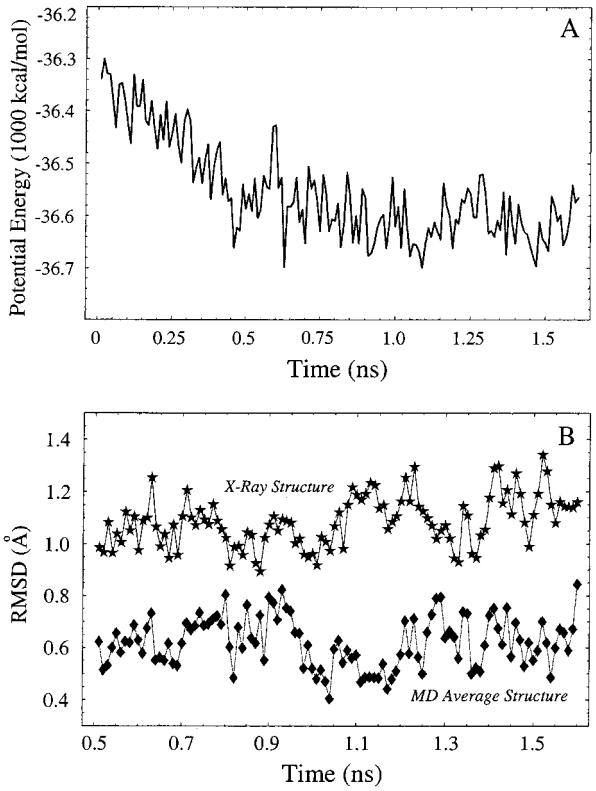

FIGURE 3: Equilibration and stability of the molecular dynamics simulation. Panel A shows that the potential energy is at equilibrium after about 0.6 ns simulation. Panel B shows that the structure does not "drift" during the equilibrium part of the simulation.

between different structures after rotation for best fits of the backbone heavy atoms (*57*):

$$\mathrm{RMSD} = \sqrt{\frac{1}{N}\sum_{i=1}^{N}(\vec{R}_i - \vec{R}_0)^2} \qquad (5)$$

where $\vec{R}_i$ and $\vec{R}_0$ describe the *x*, *y*, *z* coordinates of atoms in the comparison and reference structures, respectively. The reference structure can be an initial X-ray structure or a dynamic averaged one.

The dynamic information is inferred from the different atomic position root-mean-square fluctuation (RMSF), calculated from MD trajectories and X-ray crystallographic B factors (*57*):

$$\mathrm{RMSF}^i_{\mathrm{MD}} = \sqrt{\frac{1}{T}\sum_{t=0}^{T}(\vec{R}^i_t - \vec{R}^i_{\mathrm{ave}})^2} \qquad (6)$$

$$\mathrm{RMSF}^i_{\mathrm{X-ray}} = \sqrt{\frac{3B_i}{8\pi^2}} \qquad (7)$$

where $\vec{R}^i_t$ and $\vec{R}^i_{\mathrm{ave}}$ describe the *x*, *y*, and *z* instantaneous and time averaged coordinates of atom *i* in MD trajectories, respectively. B_i is the temperature factor for atom *i* determined from the X-ray crystallographic data.

The comparison of dynamic parameters from the MD simulation with those from NMR measurements requires the calculation of the angular reorientation correlation function $C_l(\tau)$, which, after elimination of overall molecular rotation and translation from the trajectory through rms superpostion, as above, describes the local dynamics of an

internuclear vector (e.g., N−H bond) (*38*):

$$C_I(\tau) = \langle P_2(\hat{\mu}(t)\cdot\hat{\mu}(t+\tau))\rangle \quad (8)$$

where $\hat{\mu}$ is a unit vector pointing along the N−H bond and $P_2(x) = (3x^2/2 - 1/2)$ is the second-order Legendre polynomial. The correlation functions were evaluated from the 1.1 ns trajectory using an averaging (t in eq 8) over 600 ps; hence the correlation function is defined for $0 < \tau < 0.5$ ns. The squared order parameter S^2 is defined as the long-time limit of $C_I(\tau)$

$$S^2 = \lim_{\tau\to\infty} C_I(\tau) \quad (9)$$

The sequence-specific order parameter S^2 and the fast local correlation time τ_e for a certain internuclear vector are obtained by fitting the corresponding auto correlation functions, computed from the MD trajectory data according to eq 8, to a "modelfree" function (*38*)

$$C(\tau) = S^2 + (1 - S^2)e^{-\tau/\tau_e} \quad (10)$$

The MD data was also used to compute the theoretical value of the ^{15}N R_1 relaxation rate for every site in binase. The spectral density functions necessary to carry out this computation were obtained in two ways.

In the first approach, the theoretical S^2 and τ_e for each N−H bond were obtained from fitting the autocorrelation functions (eq 8) to eq 10 to compute residue-specific "modelfree" spectral density functions,

$$J(\omega) = \frac{2}{5}\left\{\frac{S^2\tau_c}{1+\omega^2\tau_c^2} + \frac{(1-S^2)\tau_m}{1+\omega^2\tau_m^2}\right\} \quad (11)$$

where $1/\tau_m = 1/\tau_e + 1/\tau_c$, with τ_c the overall rotational correlation time.

In the second approach, as implemented in the CHARMM package, the auto correlation functions of eq 8 were multiplied with an exponential decay function describing the overall molecular tumbling, and Fourier transformed without any further assumptions about the shape of the correlation function. This process gives rise to spectral density functions of the form (*38*)

$$J(\omega) = \frac{2}{5}\left\{\frac{S^2\tau_c}{1+\omega^2\tau_c^2} + \sum_{i=1}\frac{a_i\tau_i}{1+\omega^2\tau_i^2}\right\} \quad (12)$$

allowing for multiple local motions at several time scales $\tau_{e,i}$ and (normalized) amplitudes a_i, where $1/\tau_i = 1/\tau_{e,i} + 1/\tau_c$, and $S^2 + \Sigma a_i = 1$.

The spectral density functions were used in the R_1 relaxation equation for every site assuming a 11.7 T magnetic field, a value of 6.1 ns for τ_c, and a constant value of −170 ppm for the ^{15}N CSA tensor. The results of these two approaches were identical, indicating that the local motions are generally well described by a single process.

RESULTS AND DISCUSSION

Raw Relaxation Data. Figure 4 shows all raw ^{15}N relaxation data for binase η_{xy}, {^{1}H}-^{15}N NOE, ^{15}N R_1, and ^{15}N R_2 (CPMG) and ^{15}N R_2 (echo) at two magnetic fields.

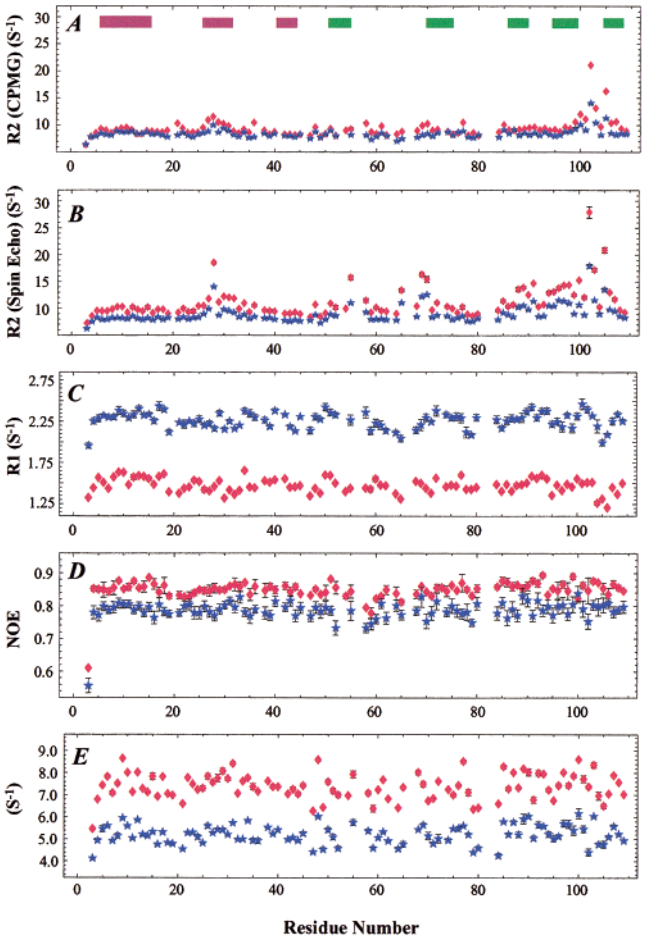

FIGURE 4: The ^{15}N relaxation data at 11.74 T (500 MHz ^{1}H) and 18.78 T (800 MHz ^{1}H) are labeled with blue asterisks and red diamonds, respectively. Error bars are indicated. Panel A shows the spin−spin relaxation rates R_2 measured using CPMG suppression of conformational exchange line broadening. Panel B shows the spin−spin relaxation rates R_2 measured using a single spin−echo to retain conformational exchange line broadening as much as possible. Panel C shows the spin−lattice relaxation rates R_1. Panel D shows the steady-state {^{1}H}-^{15}N heteronuclear NOE. Panel E shows transverse ^{15}N chemical shift anisotropy (CSA)/^{15}N-^{1}H dipole cross correlation rates (η_{xy}). The secondary structure of binase is indicated in panel A.

The differences between the two R_2 experiments show that many of the areas harboring the residues critical to the catalytic activity (e.g., the recognition loop 56−60 and the loop 99−104 containing one of the catalytic residues, His 101) are subject to conformational exchange line broadening. Using variable CPMG rates, we were able to show (*13*) that the conformational exchange dynamics occurs with a rate constant of 3000 s^{-1}, which corresponds to the maximum turn-over rate of this enzyme. Here we note that the broadening caused by this slow dynamics complicates the quantitative analysis of the ^{15}N relaxation data in terms of model free parameters.

Apart from the areas with exchange broadening, all ^{15}N relaxation data are rather flat with all measures used, and with exception of the N-terminus, does not indicate any areas with extensive fast local motions. It is to be noted, though, that several data points are missing for the loop areas around residue 65 and 80. The amide protons of residues 66 and 67 elude detection in all experiments, most likely because of excessive conformational exchange broadening. The ^{15}N

relaxation behavior of residues 81−83 cannot be accurately measured because of resonance overlap. However, by use of a HNCO-style frequency labeling (*35*), we found that the ^{15}N R_1 and R_2 relaxation for the residues in this latter loop is indistinguishable from the average, indicating that this loop is not very dynamic at any of the accessible time scales (see also Figure 9). Most significantly, the raw ^{15}N relaxation data does not show any indication of the presence of (extensive) fast local motions in the two functionally important areas in loops 56−60 and 99−104.

Rotational Anisotropy. Before data analysis in terms of order parameters can be discussed, the character of the rotational diffusion of binase in solution needs to be addressed. Figure 1 shows that binase has the shape of a prolate ellipsoid, with axis aspect ratios of 1.8:1.2:1.0. This asymmetry is expected to yield substantial variations in values of the spectral density functions and corresponding relaxation rates, depending on the directions of the associated internuclear vectors in the molecular frame. Approximating the molecule as axially symmetric, with an axis ratio 1.64:1.00, one computes with Woessner theory (*39*) a ratio of 1.5:1.0 for the rotational diffusion constants $D_{||}$ and $D_{\perp}$. Using the program HYDRONMR (*58*), which explicitly considers hydration for the computation of rotational (and translational) diffusion, we obtain the values D_{xx}, D_{yy}, and D_{zz} of 2.58, 2.12, and 1.99 $\times$ 10^7 cm^{-1} from the diagonalized diffusion tensor, at 25 C, using the X-ray coordinates (*23*). This represents an $D_{||}$ over $D_{\perp}$ ratio of 1.26. When using a variety of available coordinates, we find on average a $D_{||}$ over $D_{\perp}$ ratio 1.30 $\pm$ 0.05, where the variation reflects whether the X-ray coordinates (*23*), the NMR coordinates (*24*), or a MD-equilibrated NMR structure (this work) of binase, or NMR (*59*) or X-ray coordinates (60) of the homologous enzyme barnase (*25*, *26*) are used for the calculation. However, when computing the diffusion tensor from the experimental ^{15}N R_1 and CPMG relaxation data of the secondary structure elements, assuming that these are mostly rigid, one finds a ratio $D_{||}/D_{\perp}$ of only 1.08 $\pm$ 0.02. The variance in this number arises from several calculations using either 500 or 800 MHz data, different selections of residues, different programs (TENSOR (*61*) and MODELFREE (*44*)), and either X-ray (*23*) or NMR structure (*24*) as input. Virtually identical results ($D_{||}/D_{\perp}$ ratio of 1.1) have been obtained from NMR relaxation data for the homologous protein barnase (*62*) which has the same three-dimensional structure as binase (*25*, *26*, *59*, *60*). One may argue that the R_2 CPMG data for binase are too much affected by exchange broadening processes causing the hydrodynamic calculations based to be unreliable. One approach is to try to parse the exchange broadening from the R_2 data using transverse ^{15}N CSA/^{15}N-^{1}H dipole cross correlation rates (*32*, *60*). Regretfully, the scattering and experimental uncertainty in these values is too large to make these data usable for diffusion tensor determination (Figure 4). We thus make a simple estimation based on the R_1 values of the first two helices in the protein. Helix 6−16, in which the NH vectors point in the direction of $D_{\perp}$, has an average R_1 of 2.32 $\pm$ 0.04/1.55 $\pm$ 0.06 s^{-1} (11.74 T/18.78 T), whereas the helix 25−32, in which the NH vectors point in the direction of $D_{||}$, has an average R_1 of 2.21 $\pm$ 0.07/1.42 $\pm$ 0.07 s^{-1} (11.74 T/18.78 T). Using the Woessner axially symmetric model (*39*), one computes from the R_1 ratios at 18.78 T an axis ratio of 1.27 $\pm$ 0.17, and from the R_1 ratios at 11.74 T an axis ratio of 1.15 $\pm$ 0.10. It should be realized that when using R_1 data alone for such calculations, one assumes that the helices have identical local dynamical behavior, which may or may not be true, and which may account for the differences between the field strengths. For all used measures, thus, we find that the hydrodynamic shape of the protein is substantially more globular than suggested from the coordinates. This discrepancy is not caused by a difference in average solution structure and crystal structure, as these superimpose closely (*22*−*24*). The hydrodynamic shape is not affected by transient aggregation either, as we have found the average ^{15}N $R_{1\rho}$ relaxation rate and thus the correlation time of binase (6.1 ns at 30 °C) to be completely independent of concentration in the range 2−0.1 mM at this temperature (results not shown).

The ^{15}N relaxation data (Figure 4) unambiguously demonstrate that the first five residues of binase are dynamically disordered; moreover, the comparison of ^{13}C and ^{15}N relaxation data (Figure 10) indicates that the first three residues (6−8) of the first helix fray. Hence, the average position of the N-terminus is likely much more exposed and pointed toward solution than suggested in the X-ray structure of Figure 1. With HYDRONMR (*58*), we find that a more exposed position of this terminus causes a significant change in hydrodynamic properties of the seemingly elongated binase toward a more isotropic particle. We obtain a ratio $D_{||}/D_{\perp}$ of 1.22 when residues 1−5 are pointing out into solution. It is likely that dynamical geometry changes in the large exposed loop 56−70 could also affect the hydrodynamic shape of the molecule. These effects combined likely explain binase's lack of anisotropy as measured by the ^{15}N relaxation data.

^{15}N Order Parameters. The directional variation in spectral density functions lies between $\pm$ 2% (TENSOR and MODELFREE using all relaxation data) and $\pm$ 6% (most extreme case using 18.78 T R_1 data only). We decided to neglect this variation, and we computed the ^{15}N order parameters using the Lipari-Szabo formalism for an isotropically diffusing molecule (*38*). This approximation is justified as we are interested in much larger effects and discrepancies than could be caused by a neglect of an (unknown) degree of deviation of the spherical shape. Several combinations of the 11.74 and 18.78 T data, using all five motional models in the MODELFREE (*44*) program were made. We found that use of exclusively 18.78 T data resulted in unacceptably poor convergence for many of the residues no matter what models were used. The 11.74 T data alone do converge satisfactorily, and so does a combination of all 11.74 T data and the 18.78 T NOE and R_1 data. This points to serious problems with the R_2 data of the protein at 18.78 T, where the exchange broadening is exacerbated, apparently be it with or without CPMG suppression. We present in Figure 5 the complete MODELFREE results of the calculation with 11.74 T data only, and include the order parameters obtained by using the above-mentioned combination of 11.74 and 18.78 T data. The results do differ in detail between these calculations, but the main result is that according to the ^{15}N relaxation measurements, there is relatively little spread in order parameters over the protein. The ^{15}N order parameters do display some correlation with high order parameters for the secondary structure elements and low order parameters

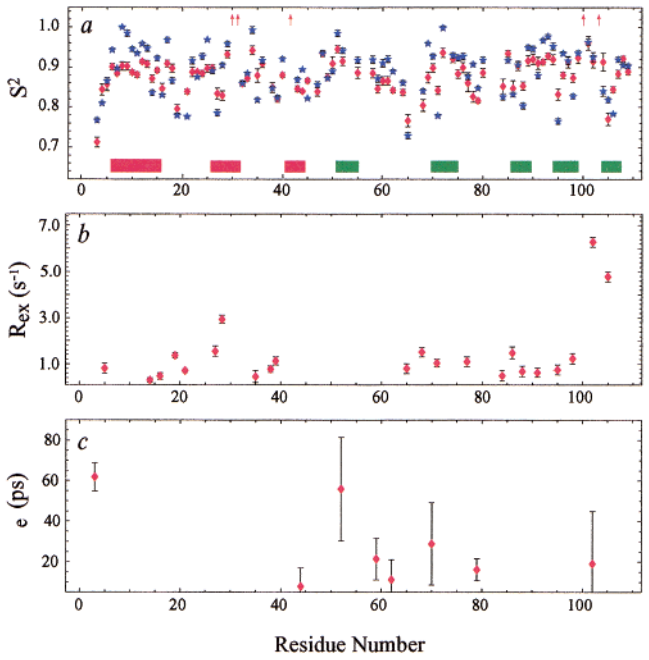

FIGURE 5: The Lipari-Szabo dynamic parameters obtained by fitting the ^{15}N R_1, R_2 and NOE data, with the program Modelfree (*44*). Order parameters S^2 are shown in red diamonds for calculations using exclusively the 11.74 T R_1, R_2(CPMG), and NOE data and in blue asterisks using the 11.74 T R_1, R_2(CPMG), and NOE data and 18.78 T R_1 and NOE data. The conformational exchange terms R_{ex} and local correlation times τ_e are shown in panels b and c for the 11.74 T data only. The secondary structure elements are indicated. Residues that could not be fitted into any of the five dynamic models for the 11.74 T data, are indicated by arrows at the top of panel a.

for loops, especially in the N-terminal region of the protein. However, almost the opposite appears to be the case in the C-terminal β-sheet domain, where lower order parameters are found especially at the N-termini of the β-strands, and where the intervening loops between the third and fourth, and fourth and fifth β-strand, have high order parameters. The literature reports varying correlation between order parameter and secondary structure. Early work on Staphylococcal nuclease finds that the "values of the order parameter are completely independent of secondary structure" (*63*). In a recent study of the vnd/NK-2 homeodomain, the average order parameters for the internal loops are equal to those of the helices (*64*). A recent study of calcium vector protein (*65*) does show a clear correlation between secondary structure and order parameters, but the order parameters in the interior loops differ only little from those in the helices (0.85 vs 0.9). At the other extreme, one finds that most of the loops in ribonuclease H (*66*) and HEW lysozyme (*67*) do show reduced order parameters, although some exceptions are seen. Most relevant for binase is that only very little pico-nano second motion is detected by NH relaxation for the enzyme's active site region consisting of the recognition loop 56−60 and catalytic loop 99−104. Five residues (Ser 30, Ala 31, Ala 42, Asp 100, and Thr 104) indicated by the arrows on top of panel a cannot be fitted into any of the five models used in the program. Three residues (Gln 28, Ala 103, and Phe 105) were found to be affected by extensive conformational exchange effects (R_{ex}). This is compatible with the conclusion drawn from the comparison of CPMG and spin−echo R_2 data in Figure 4, although the latter data

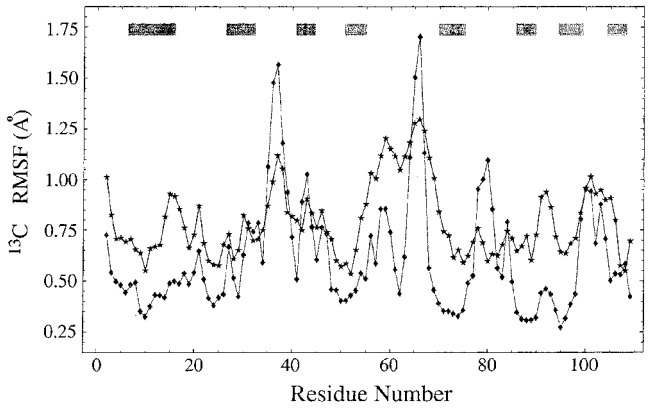

FIGURE 6: Comparison of backbone dynamics obtained from the molecular dynamics simulation (this study; diamonds) and X-ray crystallographic *B* factors (from ref 23; asterisks). The secondary structure elements are indicated.

is much more complete (see also ref *13*). Because the differences between the 11.74 and 18.78 T data are of no consequence to the overall dynamical characterization of binase, we confine our further discussion and comparisons to the 11.74 T data only.

Comparison of MD and X-ray Data. Figure 6 shows the backbone fluctuations in the crystal structure of binase (*23*), as computed from the *B*-factors using the Debye−Waller equation (eq 7). This measure of dynamics does show the typical alternation of small fluctuations for the elements of secondary structure, and larger fluctuations for the intervening loops. Consequently, the correspondence with the NMR order parameters is poor. Because several of the active site recognition residues, as well as one of the catalytic residues of binase are located on such loops, the difference is not inconsequential. While the difference could be due to differences in time scale and or dynamical modes measured by the two methods, we do not believe this to be the case as follows from a comparison of the *B*-factors with a simulated molecular dynamics computation. This figure also depicts the backbone fluctuations in binase as computed (using eq 6) from the 1.1 ns molecular dynamics simulation. This simulation is described in detail in the methods. We note here that the simulation data used for comparison with experimental data were derived from the equilibrium part of the trajectory (see also Figure 3). The relative patterns in the MD and X-ray data are seen to compare favorably for most areas (overall correlation coefficient is 0.622), except for the area around residue 15, where the *B*-factors indicate rather large fluctuations and the MD simulation not, and in the area around residue 80, where the case is reversed.

The latter situation is easily explained: the loop around residue 80 is involved in a dimer contact in the crystal (*23*) and motions could be easily quenched in that medium. We cannot offer an explanation for the former case. Thus, with this one exception, the correspondence between X-ray and MD data is good, strongly suggesting that the variations in *B*-factors above the "baseline" are caused by localized nano-pico second motions. Conversely, the correspondence between the two results provides strong evidence that the molecular dynamics calculations are supported by an experimental measure.

Comparison of NMR and MD ^{15}N Order Parameters. The comparison is shown in Figure 7a where the ^{15}N relaxation-

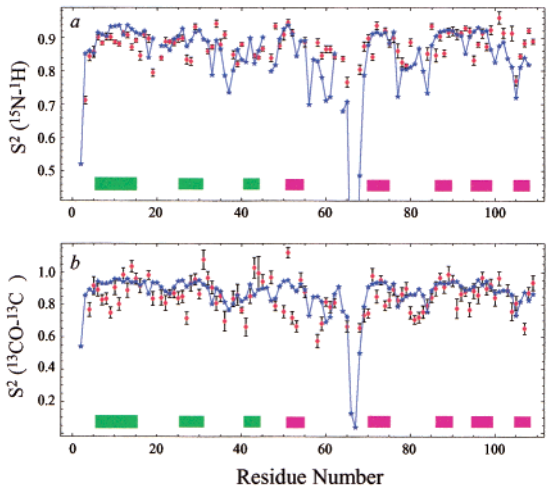

FIGURE 7: Comparisons of the experimental (red diamonds) and theoretical (blue asterisks) order parameters. S^2 (^{15}N−H) (11.74 T) and S^2 (^{13}CO−^{13}Cα) (18.78 T) are shown in panels a and b, respectively. The secondary structure elements are indicated.

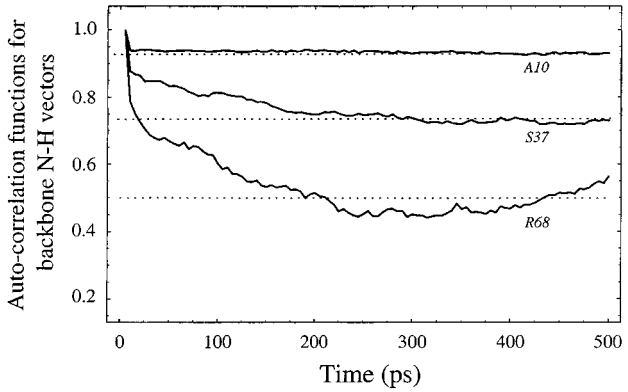

FIGURE 8: Examples of auto-correlation functions (eq 8) for N−H internuclear vectors obtained from the molecular dynamics simulation. Using eq 10, order parameters and local correlation times were fitted to values of 0.934, 1.9 ps; 0.736, 57.1 ps; and 0.486, 47.8 ps for residues 10, 37, and 68, respectively. The obtained order parameters are indicated by dashed lines.

derived order parameters (the 11.74 T data shown in Figure 5a) and those derived from the MD calculation, using eqs 8 and 9, are superimposed. As anticipated from the raw relaxation data and the discussion of the MD data above, correspondence between the experimental and theoretical order parameters is relatively poor, except for the N-terminus and the loop area 65−70. For the large majority of the residues, the MD simulated auto correlation functions decayed to a stable plateau value within 50 ps, and the theoretical order parameter could be obtained with high levels of confidence (see Figure 8). Exceptions did occur for residues 66−68, where slower motions, not fully sampled by the simulation, appear to be present as well, suggesting that the order parameter here is not well determined.

The ^{15}N order parameters of the protein barnase as obtained by others are also relatively constant over the entire protein sequence (*62*). Here, too, is it difficult to discern differences between secondary structure elements and the protein loops. Just as for binase, the barnase X-ray structure (*68*) also shows large *B*-factors in the loops corresponding very closely to the ones reported for binase (*23*). Apparently, there is a fundamental discrepancy between the different measures of dynamics, or environments, for both binase and barnase.

Potentially, this lack of correspondence could be due to problems with the ^{15}N relaxation methods for these particular proteins. The reason can be that much exchange broadening occurs in the loop areas of interest. This gives rise to a mutual cancellation of line narrowing (due to fast local motions) and line broadening (due to exchange) which would be complicating the calculations. While such occurrences could in theory be disentangled by the combined relaxation analysis of R_1, R_2, and NOE, the fact is that with a molecular weight of 12.3 kDa and a rotational correlation time of 6.1 ns, the {^{1}H}-^{15}N NOE is too close to its maximum value to be of much use, and even small experimental errors on this measurement (here ± 2%) have large effects on apparent dynamical properties. Transverse cross correlation rates could in principle help to disentangle the exchange line broadening effects, but their value is critically dependent on the magnitude and direction of the ^{15}N CSA tensor (*32*, *70*). For protein loop areas, there appears to be a consensus that these values may vary widely (*70*−*72*). Consequently, for binase where we are mostly interested in the catalytic area which consists of loops, these cross-correlation measurements are at least for now difficult to interpret for dynamical purposes.

Using ^{15}N R_1 Data for MD and NMR Comparisons. A measure not affected by these problems is the ^{15}N R_1 measurement. Provided that the data is obtained at a relatively low magnetic field (11.74 T) suspected/reported RMSD variations of ± 10 ppm in the ^{15} N CSA tensor cannot contribute to more than 2% uncertainty in the ^{15}N R_1 rates. Thus, the R_1 measurement, assuming the large molecule limit, is a reliable measure of local correlation time, its variations being caused by fast local motions only (since anisotropic overall rotation can be mostly neglected for binase). However, this relaxation, sensitive to both amplitude as well as time scale of the local motion, cannot be interpreted in a simple way (*38*).

We thus computed theoretical values for the ^{15}N R_1 relaxation from the MD simulation. We carried this out by Fourier transformation of the auto correlation function as implemented in the CHARMM program suite and as was carried out previously by others (*65*, *66*) and by fitting the computed auto-correlation functions, some of which are shown in Figure 8, to a "modelfree" shape with a single local motion (see methods). The latter was carried out to avoid over-interpretation of the potential presence of too many high frequency components in the simulated spectral density function, which would have a disproportionally large influence on the T_1 relaxation rates. We found both methods to give identical results. The theoretical and experimental ^{15}N R_1 values are shown together in Figure 9 and are found to be in somewhat better agreement with each other than the order parameters. Especially the correspondence in the catalytic residue carrying loop 99−104 and in the first α helix is better.

Nevertheless, several clear discrepancies remain in the comparison of the theoretical and experimental T_1 data, which can thus not be attributed to technical problems with the ^{15}N NMR relaxation data. One of the most salient cases is seen at the region 56−61, where the NMR data indicate motional restriction, but where the MD (and X-ray data) indicate much motion. This area of the protein is important for the biological

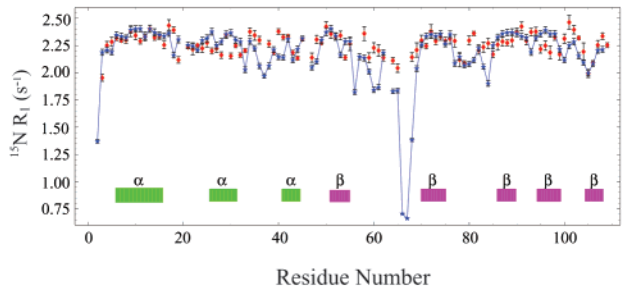

FIGURE 9: Comparison of the measured (red diamonds, 11.74 T only) and computed (blue asterisks) ^{15}N R_1. The secondary structure elements are indicated. All measured R_1 data were obtained from standard ^{15}N relaxation experiments on a ^{15}N-labeled sample, except for residues 41, 53, 54, 73, 81, 82, and 83, where HNCO-frequency labeling was used with a ^{13}C,^{15}N labeled sample.

function, as it harbors residues Arg 58 and Glu 59 that would be in contact with substrate, and neighbors Phe 55, that forms part of the nucleotide recognition site (*22*−*24*). The MD order parameters (as well as the *B*-factors, see Figure 6) indicate that Leu 62 is relatively immobile, likely caused by the fact that the side chain of this residue is tucked into the hydrophobic core of the protein. Thus, the entire loop 56−70 behaves as a pair of butterfly wings in MD and X-ray, but the first wing is motionally impaired in solution according to the ^{15}N NMR relaxation data.

Probing Pico-Nano Second Dynamics with ^{13}CO−^{13}Cα Cross Relaxation. Significantly, very much motion is detected for this area by the ^{13}CO cross relaxation data shown in Figure 7b; residue 58 actually has the lowest ^{13}CO−^{13}Cα order parameter of the entire protein. As described in detail in the methods section, the ^{13}CO−^{13}Cα cross relaxation data measures exclusively the ^{13}CO−^{13}Cα dipolar interaction, through a combination of a homonuclear {^{13}Cα}-^{13}CO NOE and a ^{13}CO R_1 measurement. The cross relaxation rate derived from these measurements is independent of the ^{13}CO CSA tensor because it is purely dipolar, and no exchange broadening is operative because it is derived from longitudinal relaxation. Since the ^{13}CO−^{13}Cα cross-relaxation is dominated by the $J(0)$ spectral density function (actually J(24 kHz)), the experiment is of high sensitivity, and it is particularly straightforward to derive the corresponding order parameter. As such, the ^{13}CO relaxation data may be a more robust measure of the order parameter than the ^{15}N relaxation. However, technical limitations in delivering selective saturation pulses also cause Cβ(i)−CO(i) and Cα (i+1)−CO(i) cross relaxation in addition to the desired Cα (i)−CO(i) cross relaxation to affect the measurements at the levels of 5 and 5.7%, respectively. In addition, all other aliphatic ^{13}C nuclei are saturated as well. On the basis of the structure of binase, we calculate that a $1/r^6$ sum of all these nuclei will produce an additional 5% increase in cross relaxation. In total, corrections of 10 and 15% for Gly and non-Gly residues, respectively, were made to the ^{13}CO data. In addition, the CO−Cα bond lengths in the binase crystal structure are significantly different for Gly and other residues (1.500 and 1.524 Å, respectively) which may call for an additional 10% correction for Gly. Because some of these corrections are invariant from residue to residue, and some are statistical, we estimate that the ^{13}CO relaxation data can currently be used with a confidence level of 90%, excluding glycines, for the assessment of *differences* in mobility along the protein backbone.

The ^{13}CO−^{13}Cα order parameter of residue 58 has the lowest value of the entire protein and its deviation from the average is clearly significant. We conclude that the ^{13}CO relaxation, in contrast to the ^{15}N order parameters, *does* detect pico/nano second mobility in this functionally important recognition loop. Apparently, fast motions are present here as well the slower motions detected by the ^{15}N linebroadening. While the latter slower motions are likely to be the functionally important ones for substrate release (*13*), it is not unreasonable to find that a general flexibility at more time scales might facilitate the adaptability of the loop for substrate recognition. The concurrence of fast and slow dynamics in loops has been observed by others as well (*66*).

How is it possible that the fast motions in loop 55−60 are not detected by the ^{15}N relaxation? The ^{15}N order parameters are a measure of rotational motional components along axes perpendicular to the N−H bond, while the ^{13}CO order parameters are a measure of the local rotational motional components along axes perpendicular to the CO−Cα bond. As these axes are not collinear, it should in principle be expected that the ^{13}CO relaxation is sensitive to different motions than the ^{15}N relaxation. In other words, the two relaxation order parameters are not expected to correspond exactly (*36*, *37*, *47*). Nevertheless, it is surprising to find that the differences can be so large. This discrepancy also indicates that the consideration of ^{15}N relaxation data alone would severely underestimate the configurational entropy of the protein backbone for this loop (*75*, *76*). In general, the ^{13}CO order parameter tracks the secondary structure of this protein somewhat better than the ^{15}N relaxation, especially in the β sheet area. Curiously, some of the theoretical ^{15}N order parameters fit better with the ^{13}CO experimental data (area 56−61), and vice versa (area around residue 80, where the ^{15}N relaxation data are "flat" according to the HNCO-style measurements). This may indicate that force fields used in the MD calculations are currently capable of deriving where motion occurs but cannot yet predict the anisotropy correctly. Clearly, such "errors" would not impact the favorable comparison between the (isotropic) *B*-factors and the MD run.

Both MD and NMR ^{15}NH and ^{13}CO−^{13}Cα order parameters indicate that only little fast motion for the backbone of the catalytic residue His 101 exists, but the MD and X-ray derived Cα displacements (Figure 6) suggest extensive presence of fast motion. In addition, the NMR ^{15}N R_2 relaxation data indicate the presence of slower motion for this residue, even more so for its neighbor Tyr 102 (*13*). This discrepancy could be attributed to the fact that displacements sample translations rather than rotations, whereas NMR relaxation samples exclusively rotation. This may indicate that the fast motions in this loop are more of the translational type.

Helix Fraying. There are two areas of discrepancy between the ^{13}CO order parameters and all other dynamics data: the stretch 45−53, and the first half of the first α helix. Stretch 45−53 is a severely distorted β sheet, that apparently buckles in a very particular fashion. The discrepancies in the N-terminal helix can be more easily explained and supported by other data. The ^{15}N relaxation is relatively featureless in this area, while the ^{13}CO order parameter is significantly

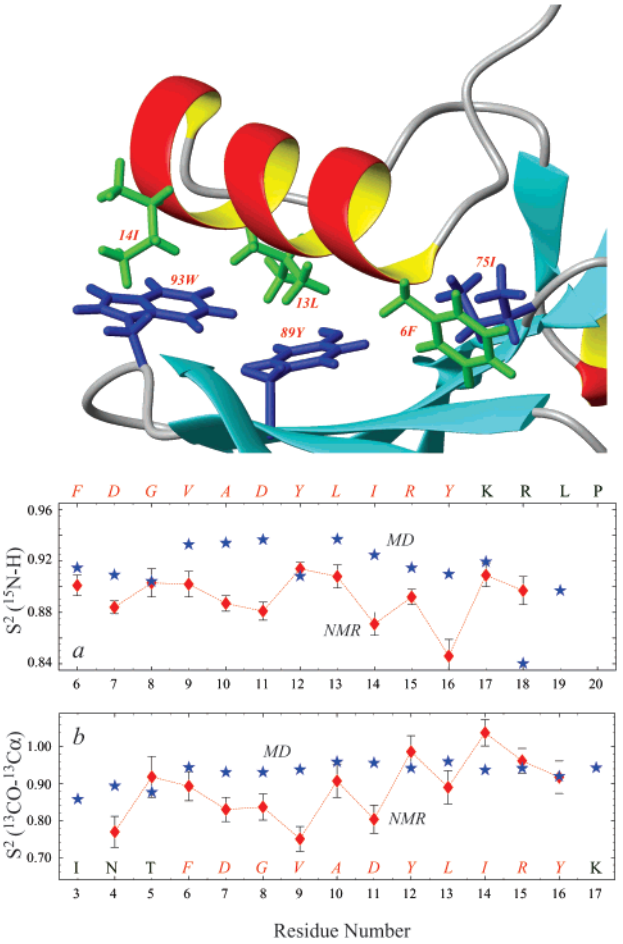

FIGURE 10: Anisotropic dynamics of the first α helix. Experimental (red diamond) and theoretical (blue asterisks) S^2 ($^{13}CO-^{13}C\alpha$) (18.78 T) and S^2 ($^{15}N-H$) (11.74 T) are shown in panels a and b, respectively. The amino acid sequence is listed. A ribbon representation of the helix is displayed above panel a, showing the interactions between the side chains of residues from the helix (green) and those from the rest of molecule (blue). The figure was prepared with the program MOLMOL (*83*).

lower for residues 4−9 than 10−15 (see Figure 10). This could indicate a rotational fraying of the N-terminus, which would not be detected by ^{15}N relaxation, as the NH vectors point with the helical axis, but would be observed by $^{13}CO-^{13}C\alpha$ dipolar relaxation as these bonds are at considerable angle (about 60 degrees) with this axis (*77*). Such motion would be allowable, because the side chains of the N-terminus of the helix, in contrast to those of the C-terminus of the helix are poorly interdigitated with the core of the protein (see Figure 10). Recent molecular dynamics folding/unfolding experiments on barnase have also suggested that the N-terminus of this helix is subject to fraying motions in the thermally unfolded state (*78*−*80*), but that the remainder of the helix is still folded even in the denatured state. Moreover, evidence was obtained from ϕ-value mutagenesis studies that the C-terminus of this helix, but not the N-terminus, is part of the transition core for the folding of the protein (*79*, *80*). Our current NMR data indicate that the fraying motions occur already at room temperature in an otherwise folded protein. It is to be noted that residue 8 is a glycine, conserved within 7 species of bacterial ribonucleases. The side chain of a residue at position 8 would be at the surface of the protein, and is not part of the interface with the natural inhibitor barstar, or substrate (*81*, *82*, *28*), so it is quite puzzling why a glycine would be conserved at this helical position. Perhaps binase has evolved to facilitate the fraying motion at the N-terminus by conserving a residue that can move more easily in φ/ψ space, allowing the remainder of the helix to form a protein folding kernel.

Significance and Conclusions. This work shows that a joint analysis of theoretical and experimental mobility data can yield additional insight in the dynamical behavior of proteins. In particular, we find that it is useful to compare ^{15}N and ^{13}C relaxation methods. Together, these furnish a more complete picture of the dynamics, which is in somewhat better agreement, for this protein, with MD simulation and with X-ray *B*-factors. Significantly, ^{15}N relaxation does not, but X-ray, MD, and ^{13}CO relaxation do, indicate the existence of extensive motion in an area that contains the residues Phe 55, Arg 58, and Glu 59, which are important to specific recognition of the substrate. By the same token, we cannot demonstrate by NMR the presence of fast motion in the loop containing the catalytic residue His 101, and the recognition residue Tyr 102, despite strong indications in MD and X-ray measurements that motions should be present. Both areas have been found to be involved in dynamics at a 300 μs time scale, which we argued to constitute the site opening rate (*13*). We speculate from all combined data that for loop 56−61 fast chain link motions underlie the slower collective opening, while the faster motions of loop 99−104 are NMR unobservable and are possibly of a more translational and concerted character. The other catalytic residue, Glu 72, is located on β2, part of the five-stranded beta sheet, that forms the "bottom" of the active site cleft. By all fast dynamical measures used in this study, the entire beta sheet is immobile with the possible exception of the N-terminus of strand β4. In our previous work (*13*), we argued that the exchange broadening effects seen for strands β3 and β4 (see Figure 4) are likely to be induced by chemical shift modulations caused by the mobile loops above it, given that residual dipolar couplings and amide proton exchange data for the sheet do suggest a rigid structure. Our present work, investigating fast dynamics, further underscores the immobility of the sheet.

Combining the results of our current and our previous work (*13*), the following dynamical characterization of the active site area of the ribonuclease binase emerges: a beta sheet, rigid at all probed time scales, supports one of the catalytic residues, Glu 72. Both substrate-encapsulating loops, L2 and L5, are mobile on both fast and slow time scales, but the fast motions of the latter loop, which contains the other catalytic residue, His 101, are not visible by NMR.

It is worthwhile to once more stress that the conclusions would have been completely different if only ^{15}N relaxation would have been considered. One would (wrongly) conclude that all areas of the active site are rigid at the nano-pico second time scale, and are all mobile at the milli-micro second time scale. Thus, the added information from ^{13}CO relaxation, MD simulation, and considering of X-ray data (this work) and residual dipolar couplings and amide proton exchange (previous work (*13*)) has modified the picture in quite a dramatic way. This work also strongly suggests that for several areas of binase, the consideration of ^{15}N relaxation data alone would severely underestimate the dynamics and thus the entropy of the protein backbone (*75*, *76*).

ACKNOWLEDGMENT

The NMR equipment was purchased with financial support from NIH, NSF, and the Keck Foundation. We thank Drs. Lincong Wang, Alexander V. Kurochkin, and Tian-Zhi Wang (Michigan) for the preparation of the labeled protein samples and for stimulating discussions, and Professor Martin Karplus (Harvard) for his hospitality and interest in this work.

REFERENCES

1. Brooks III, C. L., Karplus, M., and Pettitt, B. M. (1988) *Proteins: A Theoretical Perspective of Dynamics, Structure, and Thermodynamics*. Vol. LXXI, John Wiley & Sons: New York.
2. Kay, L. E (1998) *Nat. Struct. Biol. NMR supplement*, 513−517.
3. Zaccai, G. (2000) *Science 288*, 1604−1607.
4. Karplus, M., Evanseck, J. D., Joseph, D., Bash, P. A., and Field, M. J. (1992) *Faraday Discuss. 93*, 239−248.
5. Derreumaux, P., and Schlick, T. (1998) *Biophys J. 74*, 72−81.
6. Cox, S. M., Radzio-Andzelm, E., and Taylor, S. S. (1994) *Curr. Opin. Struct. Biol. 4*, 893−901.
7. Fitzgerald, M. M., Musah, R. A., McRee, D. E., and Goodin, D. B. (1996) *Nat. Struct. Biol. 3*, 626−631.
8. Frauenfelder, H., Parak, F., and Young, R. D. (1988) *Annu. Rev. Biophys. Biophys. Chem, 17*, 451−479.
9. Ishima, R., Freedberg, D. I., Wang, Y. X., Louis, J. M., and Torchia D. A. (1999) *Struct. Fold Des. 7*, 1047−1055.
10. Ludemann, S. K., Lounnas, V., and Wade, R. C. (2000) *J. Mol. Biol. 303*, 797−811.
11. Stuckey, J. A., Schubert, H. L, Fauman, E. B., Zhang, Z. Y., Dixon, J. E., and Saper, M. A. (1994) *Nature 370*, 571−575.
12. Juszczak, L. J., Zhang, Z. Y., Wu, L., Gottfried, D. S., and Eads, D. D. (1997) *Biochemistry 36*, 2227−2236.
13. Wang, L., Pang, Y., Holder, T., Brender, J. R., Kurochkin, A., and Zuiderweg, E. R. P. (2001) *Proc. Natl. Acad. Sci. U.S.A. 98*, 7684−7689.
14. Kay, L. E., Torchia, D. A and Bax, A. (1989) *Biochemistry 28*, 8972−8979.
15. Peng, J. W., and Wagner, G. (1994) *Nuclear Magnetic Resonance Probes of Molecular Dynamics*, R. Tycko ed., Kluwer Academic Publishers, Dordrecht, pp 373−454.
16. Palmer III, A. G., Williams, J., and McDermott, A. (1996) *J. Phys. Chem. 100*, 13293−13310.
17. Fischer, M. W. F., Majumdar, A., and Zuiderweg, E. R. P. (1998) *Prog. Nucl. Magn. Reson. Spectr. 33*, 207−72.
18. Lipari, G., Szabo, A., and Levy, R. M. (1982) *Nature 300*, 197−198.
19. Brunne, R. M., Berndt, K. D., Guntert, P., Wuthrich, K., and van Gunsteren, W. F. (1995) *Proteins 23*, 49−62.
20. Pfeiffer, S., Fushman, D., and Cowburn, D. (2001) *J. Am. Chem. Soc. 123*, 3021−3036.
21. Okorokov, A. L., Panov, K. I., Offen, W. A., Mukhortov, V. G., Antson, A. A., Karpeisky, M. Y., Wilkinson, A. J., and Dodson, G. G. (1997) *Protein Eng. 10*, 273−278.
22. Pavlovsky, A. G., Vagin, A. A., Vainstein, B. K., Chepurnova, M. K., and Karpeisky, M. Y. (1983) *FEBS Lett. 162*, 167−70.
23. Dodson, G. G., personal communication.
24. Reibarkh, M. Ya., Nolde, D. E., Vasilieva, L. I., Bocharov, E. V., Shulga, A. A., Kirpichnikov and M. P., and Arseniev, A. S. (1998) *FEBS Lett. 431*, 250−254.
25. Hill, C., Dodson, G., Heinemann, U., Saenger, W., Mitsui, Y., Nakamura, K., Borisov, S., Tischenko, G., Polyakov, K., and Pavlovsky, S. (1983) *Trends Biochem. Sci. 8*, 364−369.
26. Schulga, A., Kurbanov, F., Kirpichnikov, M., Protasevich, I., Lobachov, V., Ranjbar, B., Chekhov, V., Polyakov, K., Engelborghs, Y., and Makarov, A. (1998) *Protein Eng. 11*, 775−782.
27. Okorokov, A. L., Panov, K. I., Kolbanovskaya, E. Y., Karpeisky, M. Y., Polyakov, K. M., Wilkinson, A. J., and Dodson, G. G. (1996) *FEBS Lett. 384*, 143−146.
28. Buckle, A. M., and Fersht, A. R. (1994) *Biochemistry 33*, 1644−1653.
29. Petsko, G. A., and Ringe, D. (1984) *Annu. Rev. Biophys. Bioeng. 13*, 331−371.
30. Philippopoulos, M., and Lim, C. (1995) *J. Mol. Biol. 254*, 771−792.
31. Chatfield, D. C., Szabo, A., and Brooks, B. R.(1998) *J. Am. Chem. Soc. 120*, 5301−5311.
32. Tjandra, N., Szabo, A., and Bax, A. (1996) *J. Am. Chem. Soc. 118*, 6986−6991.
33. Meiboom, S., and Gill, D. (1954) *Rev. Sci. Instr. 29*, 688−691.
34. Kay, L. E., Nicholson, L. K., Delaglio, F., Bax, A., and Torchia, D. A. (1992) *J. Magn. Reson. 97*, 359−375.
35. Caffrey, M., Kaufman, J., Stahl, S. J., Wingfield, P. T., Gronenborn, A. M., and Clore, G. M. (1998) *J. Magn. Reson. 135*, 368−372.
36. Zeng, L., Fischer, M. W. F., and Zuiderweg, E. R. P. (1996) *J. Biomol. NMR, 7*, 157−162.
37. Fischer, M. W. F., Zeng, L., Pang, Y., Hu, W., Majumdar, A., and Zuiderweg, E. R. P. (1997) *J. Am. Chem. Soc. 119*, 12629−12642.
38. Lipari, G., and Szabo, A. (1982) *J. Am. Chem. Soc. 104*, 4546−4558.
39. Woessner, D. E. (1962) *J. Chem. Phys. 37*, 647−654.
40. Delaglio, F., Grzesiek, S., Vuister, G. W., Zhu, G., Pfeifer, J., and Bax, A. (1995) *J. Biomol. NMR 6*, 277−293.
41. Johnson, B. A., and Blevins, R. A. (1994) *J. Biomol. NMR 4*, 603−614.
42. Devore, J. L, (1995) *Probability and Statistics for Engineering and the Sciences*, Duxbury Press, Belmont.
43. Press, W. H., Teukolsky, S. A., Vetterling, W. T., and Flannery, B. P. (1997) *Numerical Recipes in C*, 2nd ed., Cambridge University Press, New York.
44. Mandel, A. M., Akke, M., and Palmer III, A. G. (1995) *J. Mol. Biol. 246*, 144−163.
45. Brooks, B. R., Bruccoleri, R. E., Olafson, B. D., States, D. J., Swaminathan, S., and Karplus, M. (1983) *J. Comput. Chem. 4*, 187−217.
46. , MacKerell, Jr., A. D., Bashford, D., Bellott, M., Dunbrack, Jr., R. L., Evanseck, J. D., Field, M. J., Fischer, S., Gao, J., Guo, H., Ha, S., Joseph-McCarthy, D., Kuchnir, L., Kuczera, K., Lau, F. T. K., Mattos, C., Michnick, S., Ngo, T., Nguyen, D. T., Prodhom, B., Reiher, III, W. E., Roux, B., Schlenkrich, M., Smith, J. C., Stote, R., Straub, J., Watanabe, M., Wirkiewicz-Kuczera, J., Yin, D., and Karplus, M. (1998) *J. Phys. Chem. B 102*, 3586−3616.
47. Buck, M., and Karplus, M. (1999) *J. Am. Chem. Soc. 121*, 9645−9658.
48. Loncharich, R. J., and Brooks, B. R. (1989) *Proteins: Struct. Funct. Genet. 6*, 32−45.
49. Jorgensen, W. L., Chandrasekhar, J., Madura, J. D., Impey, R. W., and Klein, M. L (1983). *J. Chem. Phys. 79*, 926−935.
50. Neria, E., Fischer, S., and Karplus, M. (1996) *J. Chem. Phys. 105*, 1902−1921.
51. Brooks, C. L., and Karplus, M. (1983) *J. Chem. Phys. 79*, 6312−6325.
52. Rychaert, J.-P., Ciccotti, G., and Berendsen, H. J. C (1979). *J. Comput. Phys. 23*, 327−341.
53. Nose, S. (1984) *J. Chem. Phys. 81*, 511−519.
54. Hoover, W. G. (1985) *Phys. Rev. A, 31*, 1695−1697.
55. Tuckerman, M. E., Berne, B. J., and Martyna, G. J. J. (1992) J. Chem. Phys. *97*, 1990−2001.
56. Watanabe, M., and Karplus, M. (1995) *J. Phys. Chem. 99*, 5680−5697.
57. Elofsson, A., and Nilsson, L. (1996) *J. Phys. Chem.. 100*, 2480−2488.
58. De la Torre, J. C., Huertas, M. L., and Carrasco, B. (2000) *J. Magn. Reson. 147*, 138−146.
59. Bycroft, M., Ludvigsen, S., Fersht, A. R., and Poulsen, F. M. (1991) *Biochemistry 30*, 8697−8701.
60. Mauguen, Y., Hartley, R. W., Dodson, E. J., Dodson, G. G., Bricogne, G., Chothia, C., and Jack, A. (1982) *Nature 297*, 162−164.

61. Dosset, P., Hus, J.-C., Blackledge, M., and Marion, D. (2000) *J. Biomol NMR, 16*, 23−28.
62. Sahu, S. C., Bhuyan, A. K., Udgaonkar, J. B., and Hosur, R. V. (2000) *J. Biomol NMR 18*, 107−118.
63. Kay, L. E., Torchia, D. A., and Bax, A. (1989) *Biochemistry 28*, 8972−8979.
64. Fausti, S., Weiler, S., Cuniberti, C., Hwang, K.-J., No, K. T., Gruschus, J. M., Perico, A., Nirenberg, M., and Ferretti, J. A. (2001) *Biochemistry 40*, 12004−12012.
65. Theret, I., Baladi, S., Cox, J. A, Gallay, J., Sakamoto, H., and Craescu, C. T. (2001) *Biochemistry 40*, 13888−13897.
66. Mandel, A. M., Akke, M., and Palmer, A. G., III, (1996) *Biochemistry 35*, 16009−16023
67. Buck, M., Boyd, J, Redfield, C., MacKenzie, D. A., Jeenes, D. J., Archer, D. B., and Dobson, C. M. (1995) *Biochemistry 34*, 4041−4055.
68. Kroenke, C. D., Loria, J. P., Lee, L. K., Rance, M., and Palmer, A. G, III, (1998) *J. Am. Chem. Soc. 120*, 7905−7915.
69. Meiering, E. M., Serrano, L., and Fersht, A. R. (1992) *J. Mol. Biol. 225*, 585−589.
70. Kroenke, C. D., Rance, M., and Palmer III, A. G. (1999) *J. Am. Chem. Soc. 121*, 10119−10125.
71. Fushman, D., Tjandra, N. and Cowburn, D. (1998) *J. Am. Chem. Soc. 120*, 10947−10952.
72. Canet, D., Barthe, P., Mutzenhardt, P., and Roumestand, C. (2001) *J. Am. Chem. Soc. 123*, 4567−4576.
73. Eriksson, M. A., Berglund, H., Hard, T., and Nilsson, L. (1993) *Proteins 17*, 375−390.
74. Smith, P. E., van Schaik, R. C., Szyperski, T., Wuthrich, K., and van Gunsteren W. F. (1995) *J. Mol. Biol. 246*, 356−365.
75. Akke, M., Brüschweiler, R. and Palmer, A. G., III (1993) *J. Am. Chem. Soc. 115*, 9832−9833.
76. Yang, D., and Kay, L. E. (1996) *J. Mol. Biol. 263*, 369−382.
77. Fischer, M. W. F., Zeng, L., Majumdar, A., and Zuiderweg, E. R. P. (1998) *Proc. Natl. Acad. Sci. U.S.A. 95*, 8016−8019.
78. Caflisch, A., and Karplus, M. (1995) *J. Mol. Biol. 252*, 672−708.
79. Bond, C. J., Wong, K. B., Clarke, J., Fersht, A., and Daggett, V. (1997) *Proc. Natl. Acad. Sci. U.S.A. 94*, 13409−13413.
80. Li, A., and Daggett, V. (1998) *J. Mol. Biol. 275*, 677−694.
81. Guillet, V., Lapthorn, A., Hartley, R. W., and Mauguen, Y. (1993) *Structure 1*, 165−176.
82. Buckle, A. M., Schreiber, G., and Fersht, A. R. (1994) *Biochemistry 33*, 8878−8889.
83. Koradi, R., Billeter, M., and Wüthrich, K. (1996) *J. Mol. Graph. 14*, 51−55.
84. Kay, L. E., Keifer, P. and Saarinen, T (1992) *J. Am. Chem. Soc. 114*, 10663−10664.
85. Zhu, G., Xia, Y., Nicholson, L. K., and Sze, K. H. (2000) *J. Magn. Reson. 143*, 423−426.
86. Palmer III, A. G., Kroenke, C. D., and Loria, J. P. (2001) *Methods Enzymol. 339*, 204−238.

BI011657F